Proceedings of 2004 Korea-Japan Joint Seminar
on Particle Image Velocimetry
POSTECH, Korea, Dec. 9 – 10

Sub-pixel image interpolations for PIV

Byoung Jae Kim and Hyung Jin Sung

Department of Mechanical Engineering,
Korea Advanced Institute of Science and Technology,
Guseong-dong, Yuseong-gu, Daejeon, 373-1, Korea
hjsung@kaist.ac.kr

Abstract: Several interpolations for image deformation in PIV were evaluated. The tested interpolation methods are linear, quadratic, truncated sinc, windowed sinc, cubic, Lagrange, Gaussian 2nd and 6th interpolators. Bias errors and random errors were evaluated in the range of 0~3.0 pixel uniform displacement using synthetic images. We also measured the time cost of each interpolator with respect to kernel size. The cubic interpolator with 6×6 kernel showed the best results in terms of the performance and time cost.

Keywords: PIV, image deformation, interpolator, bias error, random error

1. Introduction

PIV (particle image velocimetry) has been a main tool to measure the instantaneous velocity map using cross-correlation of two consecutive particle images. The cross-correlation accelerated by FFT, as its conventional algorithm, has many limitations in strong-velocity-gradient flows because of the fixed location and size of two interrogation windows. To overcome this, some advanced techniques in image processing have been developed ([1]~[9]).

Huang et al (1993) proposed PID(particle image distortion), according to flow patterns, to improve the limitations in the conventional cross-correlation where the velocity gradient is high. The process started with a conventional cross-correlation. The resultant velocity distribution was then used to shift and deform the interrogation windows to compensate for particle-pair loss due to in-plane and out-of-plane motions. Scarano(2000) applied the multigrid technique that reduces the window size successively in accordance with previous result to PID, and accordingly obtained more high spatial resolution than the original PID.

Tokumaru and Dimotakis (1995) gave a general approach to the problem of matching from fluid motion. The spatial cross correlation was viewed as an optimization process performed in the space of the displacement components. They proposed to enlarge the dimensionality of the optimization domain introducing the spatial derivatives of the displacement distribution as independent parameters. Accordingly, the correlation peak corresponds to parameters's values describing the local velocity and its derivatives. Scarano (2004) added the multigrid to second derivatives correlation.

These techniques are based on the processing of continuous images, which are obtained by interpolating(re-sampling) digital images. In PIV, because the interpolation for pixel intensity at a sub-pixel location is ahead of non-linear image processing to extract a vector, the performance of PIV could depend greatly on what kind of interpolation is adopted. Huang et al (1993) adopted linear interpolation for PID and 0.25 pixel uncertainty was showed. Tokumaru and Dimotakis (1995) also used the same interpolation for the 2nd order of the series expansion process in experiments. Instead, Scarano(2000, 2002, 2004) selected truncated sinc interpolation that is more

complicate than linear interpolation for window deformation. Fincham and Delerce (2000) used 2D-spline interpolation and indicated the weak reflection of true distribution beneath the scale of 1 pixel.

Since the deformation of the 2nd interrogation window is described as a continuous 2D plane, we must know the pixel intensity at a sub-pixel location in the deformed window, which is realized through a kind of interpolation. An interpolator has been however intuitively selected for realizing continuous image, without quantitative any information on the interpolation performance. Therefore, the objective of this study is to quantitatively evaluate and compare the performance and the time cost of interpolators. Several interpolators and their characteristics (linear, truncated sinc, windowed sinc, quadratic, cubic, Gaussian, Lagrange interpolations) were introduced. The tested PIV algorithm is the 1st order deformation proposed by Huang et al (1993), because some techniques are similar or succeed to that algorithm[2-5]. For the exact evaluation, computer synthetic images were generated ($\overline{d}_p = 2$ and $\sigma_p = 1$). There may be many criteria, such as bias and random errors according to uniform displacement or linear shear, and the frequency response by sinusoidal motions. In this paper, however, only bias and random errors with respect to uniform displacement (0~3.0 pixel) were dealt with for each interpolator with different kernel sizes (2×2 to 10×10). Besides these errors, the time costs were also measured and analyzed.

2. Window deformation

2.1 Cross-correlation matching

Several techniques for determining flow velocities from particle image pair employ an optimization that relies on some form of a cross-correlation function, e.g. ,

$$\max_{a} \int_{A} f_1(\mathrm{x}) f_2(\mathrm{x}+\mathrm{a}) \mathrm{dx}^2 , \tag{1}$$

where the displacement a is a vector to be determined by the optimization procedure and A is the correlation domain. The intensity distribution of the image, $f(\mathrm{x})$, is known at times t_1 and t_2; i.e., $f_1(\mathrm{x})$ and $f_2(\mathrm{x})$. A first-order approximation of the displacement in the neighborhood of x_0 is expressed through a Taylor series truncated at the linear term ,

$$\mathrm{a} = \mathrm{a}(\mathrm{x}) = \mathrm{a}(\mathrm{x}_0) + (\nabla \mathrm{a})_0 (\mathrm{x} - \mathrm{x}_0) , \tag{2}$$

The conventional cross-correlation analysis can be referred to as a zero-order matching approximation. Instead, Eq.(1) with the displacement distribution of Eq.(2) is referred to as a first-order approximation(Fig.1). The main purpose of this operation is to achieve matching between regions where the continuum deformation is accounted for, in terms of translation, rotation, shearing and dilation.

2.2 Interpolation

Deformation process needs image re-sampling in order to obtain particle intensity information at sub-pixel locations in f_2 image for Eq.(1). Interpolation for the re-sampling can be described formally as the convolution of the discrete image samples, $f(m,n)$, with the continuous 2D impulse response ${}_{2D}h(x,y)$ of a 2D reconstruction filter[10],

$$f(x,y) = \sum_m \sum_n f(m,n) \cdot {}_{2D}h(m-x, n-y) , \tag{3}$$

where $f(x,y)$ represents the image intensity retrieved at a sub-pixel location. Usually, symmetrical and separable interpolation kernels are used to reduce the computation complexity,

$${}_{2D}h(x,y) = h(x)h(y) . \tag{4}$$

Following the sampling theory, the original image $f(x,y)$ can be reconstructed perfectly from its samples $f(m,n)$ by multiplication of an appropriate rectangular prism in the Fourier domain.

The 1D ideal interpolation equals the multiplication with a rect function in the Fourier domain and can be realized in the spatial domain by a convolution with sinc function,

$$^{ideal}h(x) = \frac{\sin(\pi x)}{\pi x} = \mathrm{sinc}(x). \tag{5}$$

Some fundamental properties of any interpolator can be derived from this ideal interpolation function. $^{ideal}h(x)$ is positive from zero to one, negative from one to two, positive from two to three, and so on. For $h(0)=1$, these zero crossings guarantee that the image is not modified if it is re-sampled on the same grid. Therefore, kernels satisfying

$$\begin{cases} h(0)=1 \\ h(x)=0, |\, x \,| = 1,2,... \end{cases} \tag{6}$$

avoid and preserve high frequencies. They are called interpolators.

Particularly, the sum of all samples should be one for any displacement $0 \le d < 1$,

$$\sum_{m=-\infty}^{\infty} h(d+m) = 1. \tag{7}$$

This means that for any displacement d the direct current (DC) amplification will be unity and the energy of the re-sampled image remains unchanged (DC-constant). In other words, the mean brightness of the image is not affected if the image is interpolated or re-sampled[10].

$$\sum_{m=-\infty}^{\infty} h(d+m) = 1 \Leftarrow \begin{cases} H(0)=1 \\ H(f)=0, |\, f \,| = 1,2,... \end{cases} \tag{8}$$

The conditions in Eq.(8) are not sufficient but necessary in the context of interpolation. Below are some $h(x)$ with kernel size N.

- Truncated sinc interpolator

$$_{\mathrm{sinc}}h_N = \begin{cases} ^{ideal}h(x), & 0 \le |\, x \,| < N/2 \\ 0, & \text{elsewhere} \end{cases} \tag{9}$$

- Windowed sinc interpolator (Blackman-Harris window)

$$_{\mathrm{wsinc}}h_N = \begin{cases} ^{ideal}h(x) \cdot w(x), & 0 \le |\, x \,| < N/2 \\ 0, & \text{elsewhere} \end{cases} \tag{10}$$

where $w(x) = 0.42323 + 0.49755\cos(2\pi x/N) + 0.07922\cos(4\pi x/N)$

- Linear interpolator

$$_{\mathrm{linear}}h = \begin{cases} 1-|\, x \,|, & 0 \le |x| < 1 \\ 0, & \text{elsewhere} \end{cases}, \tag{11}$$

- Quadratic interpolator ($a=1$)

$$_{\mathrm{linear}}h = \begin{cases} -2a\,|\, x \,|^2 + \dfrac{a+1}{2}, & 0 \le |\, x \,| < \dfrac{1}{2} \\ +a\,|\, x \,|^2 - \dfrac{2a+1}{2}\,|\, x \,| + \dfrac{3(a+1)}{4}, & \dfrac{1}{2} \le |\, x \,| < \dfrac{3}{2}, \\ 0, & \text{elsewhere} \end{cases} \tag{12}$$

- Cubic interpolator ($a=-0.5$)

$$ {}^{\text{cubic}}h_2 = \begin{cases} 2|x|^3 - |x|^2 + 1, & 0 \le |x| < 1 \\ 0, & \text{elsewhere} \end{cases} \tag{13} $$

$$ {}^{\text{cubic}}h_4 = \begin{cases} (a+2)|x|^3 - (a+3)|x|^2 + 1, & 0 \le |x| < 1 \\ a|x|^3 - 5a|x|^2 + 8a|x| - 4a, & 1 \le |x| < 2 \\ 0, & \text{elsewhere} \end{cases} \tag{14} $$

$$ {}^{\text{cubic}}h_6 = \begin{cases} \frac{6}{5}|x|^3 - \frac{11}{5}|x|^2 + 1, & 0 \le |x| < 1 \\ -\frac{3}{5}|x|^3 + \frac{16}{5}|x|^2 - \frac{27}{5}|x| + \frac{14}{5}, & 1 \le |x| < 2 \\ \frac{1}{5}|x|^3 - \frac{8}{5}|x|^2 + \frac{21}{5}|x| - \frac{18}{5}, & 2 \le |x| < 3 \\ 0, & \text{elsewhere} \end{cases} \tag{15} $$

$$ {}^{\text{cubic}}h_8 = \begin{cases} \frac{67}{56}|x|^3 - \frac{123}{56}|x|^2 + 1, & 0 \le |x| < 1 \\ -\frac{33}{56}|x|^3 + \frac{177}{56}|x|^2 - \frac{75}{14}|x| + \frac{39}{14}, & 1 \le |x| < 2 \\ \frac{9}{56}|x|^3 - \frac{75}{56}|x|^2 + \frac{51}{14}|x| - \frac{45}{14}, & 2 \le |x| < 3 \\ -\frac{3}{56}|x|^3 + \frac{33}{56}|x|^2 - \frac{15}{14}|x| + \frac{18}{14}, & 3 \le |x| < 4 \\ 0, & \text{elsewhere} \end{cases} \tag{16} $$

▪Lagrange interpolator

$$ {}^{Lagra}h_N = \begin{cases} \prod_{j=0, j-N/2+1 \neq n}^{N-1} \frac{n-i-x}{n-i}, & n-1 \le x < n \\ 0, & \text{elsewhere} \end{cases} \tag{17} $$

where $i = j - N/2 + 1$, n : integer

▪2nd order Gaussian interpolator

$$ {}^{Gauss}h_N = \begin{cases} G^0(x, 2\gamma_2) - \gamma_2 G^2(x, \gamma_2), & 0 \le |x| < N/2 \\ 0, & \text{elsewhere} \end{cases} \tag{18} $$

where, $G^0(x,\beta) = \frac{1}{\sqrt{2\pi\beta}} e^{-x^2/2\beta}$, $\gamma_2 = \frac{1}{2\pi}\left(\frac{1}{\sqrt{2}} + 1\right) \approx 0.4638115$

▪6th order Gaussian interpolator

$$ {}^{Gauss}h_N = \begin{cases} G^0(x, 2\gamma_6) - \gamma_6 G^2(x, \gamma_6) - \frac{r_6^3}{24} G^6(x, \gamma_6), & 0 \le |x| < N/2 \\ 0, & \text{elsewhere} \end{cases}, \tag{19} $$

where, $\gamma_6 = \frac{1}{2\pi}\left(\frac{1}{\sqrt{2}}+1+\frac{15}{24}\right) \approx 0.8655995$

3. Results and discussion

3.1 Artificial image generation

The individual particles are described by a Gaussian intensity profile [11],

$$I(x,y) = I_0 \exp\left(-\frac{(x-x_0)^2+(y-y_0)^2}{(d_p/2)^2}\right), \tag{20}$$

where d_p and (x_0, y_0) are the diameter and the center of the tracer particle, respectively. The factor I_0 emulates the laser sheet illumination and is a function of the particle's position z within the laser sheet and the light scattering efficiency of particles, q,

$$I_0(z_0) = q \exp\left(-\frac{(z-z_0)^2}{\sigma^2}\right) \tag{21}$$

where 2σ and z_0 are the thickness and the center position of the laser sheet, respectively. In this study, particles with $\bar{d}_p = 2$ pixels and $\sigma_p = 1$ pixel were randomly generated onto 8 bit gray images. The number of particles was $C = 20000$ inside the volume of 512×512×7 ($2\sigma = 7$ pixels).

Mathematically, each pixel is assigned an intensity value as follows (Fig.2),

$$I(i,j) = \iint_A I_0 \exp\left(-\frac{(x-x_0)^2+(y-y_0)^2}{(d_p/2)^2}\right). \tag{22}$$

Here, the width and height of each pixel are 1. Following this, in the case of a pixel fully occupied by the particle like the center pixel in Fig.2, the Gaussian function is easily integrated over its rectangular area using the error function. However, the analytic treatment for partially covered pixels becomes tricky since the area of integration may turn out to be quite inconvenient. A semi-analytic method is therefore developed to compute intensity values. Each pixel under consideration is divided into 100 strips (Fig. 3). Each strip is treated as a line with equation $y = y_p + y' = y_p + k/100\,(k = 0,1,2,3,\ldots 100)$. The particle boundary would have the equation,

$$(x-x_0)^2 + (y-y_0)^2 = (d_p/2)^2. \tag{23}$$

If its intersection with the line $y = y_p + y'$ exists, the bounds of the line $y = y_p + y'$ lying within the particle image circle and the pixel are determined as l and u, which are a function of y'. Thus these values serve as the limits of integration when the integral in Eq.(22) is opened up thus,

$$I(i,j) = I_0 \int_0^1 \left[\exp\left(-\left(\frac{y-y_0}{d_p/2}\right)^2\right) \cdot \int_l^u \exp\left(-\left(\frac{x-x_0}{d_p/2}\right)^2\right) dx'\right] dy'. \tag{24}$$

Now the inner integral,

$$I(y') = \int_l^u \exp\left(-\left(\frac{x-x_0}{d_p/2}\right)^2\right) dx' = \int_l^u \exp\left(-\left(\frac{x_p+x'-x_0}{d_p/2}\right)^2\right) dx', \tag{25}$$

can be computed using the error function between limits l and u. Now the outer integral is approximated as the following sum (with $\Delta y' = 0.01$),

$$I(i,j) = I_0 \sum_{k=0}^{100} \left(I\left(\frac{k}{100}\right) \exp\left(-\left(\frac{y_p + k/100 - y_0}{d_p/2} \right)^2 \right) \right) \Delta y' \qquad (26)$$

3.2 Uniform displacement

As a peak-estimator, Gaussian fitting was used, and the validation of vectors and the replacement of error vectors were not made. The window size was set 32×32. Figures.4~10 show the bias errors of interpolation described in Eqs.(9~19), as a function of uniform displacement (0~3.0 pixel). The bias errors in most cases tend to decrease at every multiple of 0.5 pixel, showing a sinusoidal shape. This is well known as a peak-locking phenomenon, where the peak-locking mechanism is elucidated by Fincham and Spedding (1997). It is found in Fig.4 that the conventional cross-correlation and the 1st order deformation with linear or quadratic interpolations, comparatively simple methods, have not only large absolute value of bias error but also large fluctuations of bias error, compared with others. The maximum error is up to -0.06 pixel for the conventional cross-correlation, -0.03 pixel for the inear interpolation, and -0.04 pixel for the quadratic interpolation. The reason why the quadratic the interpolation works slightly worse than linear interpolation might be the discontinuity of the 1st derivation of Eq.(12) at $x = 0.5$. This discontinuity raises the kernel's stopband attenuation for high frequency above 2%. For the other interpolations, Figs.5~10 tell that the maximum bias errors converge to about -0.015 pixel when the kernel size is larger than 6×6.

The interpolators used in Figs.8~10 do not fulfill one or two conditions in Eq.(6), so strictly speaking they are not interpolators in a view of ideal interpolation like Eq.(5). The Gaussian 6th order interpolator more satisfies Eq.(6) than the Gaussian 2nd order interpolator does. Thus, the Gaussian 6th interpolator is better, as seen in Figs.8~9. One might think that the Gaussian function, such as $G^0(x,\beta)$ in Eq.(18), would be the best interpolator because a particle is modeled as a Gaussian function, as mentioned in Eqs.(20)~(21). This assumption would be right if the diameter of all particles could be known. But if even so, it is unfortunately impossible because the problem happens in satisfying Eq.(6). The Lagrange interpolator is one of the most frequently used fitting schemes in mathematics. The fitting curve with $N-1$ degree of polynomials is made so that it must pass through N points. Hence, this does not mostly fulfill Eq.(6). Unlike the other interpolator, there is no evident convergent tendency of bias error according to N, which might be caused by the relatively large change of the fitting curve with N due to its innate characteristics.

Figures.11~14 compare graphically bias and random errors of different interpolators. Here, each performance line is taken from each interpolation with the best kernel size. The mean value and standard deviation of each performance line in Figs.8~9 are tabulated in Table.1. We can see that there is no difference in the mean value, but big difference in the standard deviation. From these results, the windowed sinc and cubic interpolators are good for uniform flows in terms of error performance. In addition to the error performance, time cost for each interpolation in 1024×1024 pixel^2 were measured and summarized in Table.2. It is shown that the interpolators having kinds of polynomials work faster. Through this table, it can be concluded in uniform displacement that the cubic interpolator with kernel size 6×6 is reasonable and recommendable in terms of the error performance and computational time.

4. Future plan and conclusions

The bias and random errors of interpolations for the 1st order image deformation in PIV were investigated. The results show that the cubic interpolation with 6×6 kernel size is the most effective scheme in uniform displacement. In the range of 0~3.0 pixel uniform displacement, the bias error was less than about -0.015 pixel and the random error was about 0.02 pixel. To examine the effects of interpolators more, we are going to test them in linear shear and sinusoidal motions. Moreover, the more practical process, deformation with mutigrid, will be applied to turbulent flows, changing interpolators.

References

[1] Huang H.T., Fiedler H.E. and Wang J.J., "Limitation and improvement of PIV," Experiments in Fluids 15 (1993) 168.

[2] Scarano F. and Riethmuller M.L., "Advances in iterative multigrid in PIV image processing," Experiments in Fluids suppl. (2000) 51.

[3] Tokumaru P.T. and Dimotakis P.E., "Image-correlation velocimetry," Experiments in Fluids 19 (1995) 1.

[4] Scarano F., "A super-resolution particle image velocimetry interrogation approach by means of velocity second derivatives correlation," Measurement Science & Technology 15 (2004) 475.

[5] Scarano F., "Iterative image deformation methods in PIV," Measurement Science & Technology 13 (2002) R1.

[6] Fincham A. and Delerce G., "Advanced optimization of correlation image velocimetry algorithms," Experiments in Fluids suppl. (2000) 13.

[7] Fincham A.M. and Spedding G.R., "Low cost, high resolution DPIV for measurement of turbulent fluid flow," Experiments in Fluids 23 (1997) 23.

[8] Wereley S.T. and Gui L., "A correlation-based central difference image correlation (CDIC) method and application in a four-roll mill flow PIV measurement," Experiments in Fluids 34 (2003) 42.

[9] Hart D.P., "PIV error correction," Experiments in Fluids 29 (2000) 13.

[10] Lehmann T.M., Gonner C., Spitzer K., "Survey: Interpolation methods in medical image processing," IEEE Transactions on medical imaging 18 11 (1999), 1049.

[11] Okamoto K., Nishio S., Saga T. and Kobayasi T., "Standard images for particle-image velocimetry," Measurement Science & Technology 11 (2000), 685.

	kernel size (N)	mean (pixel)	standard deviation (pixel)
truncated sinc	6×6	-0.00904	0.00481
windowed sinc	8×8	-0.00917	0.00237
cubic	6×6	-0.00916	0.00248
Gaussian 6th	6×6	-0.00907	0.00296
Lagrange	4×4	-0.00922	0.00423

Table 1 Comparison of bias errors of interpolators in Figs.11~12 (uniform displacement)

	2×2	4×4	6×6	8×8	10×10
linear	4				
sinc	5	10	17	25	38
windowed sinc	8	18	34	60	91
Cubic	5	8	14	23	
Gaussian 6th	13	40	81	150	226
Lagrange	=linear	11	26	49	80

Table 2 Time cost with respect to kernel size for some interpolators (unit: second)

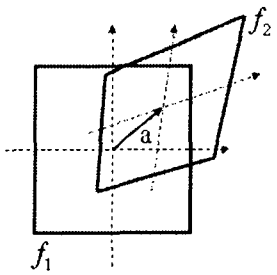

Fig. 1 Window transformation of the particle image

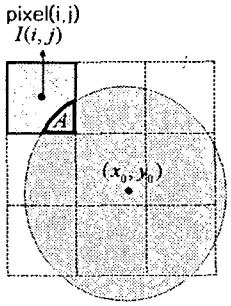

Fig. 2 Intensity assignment of a pixel

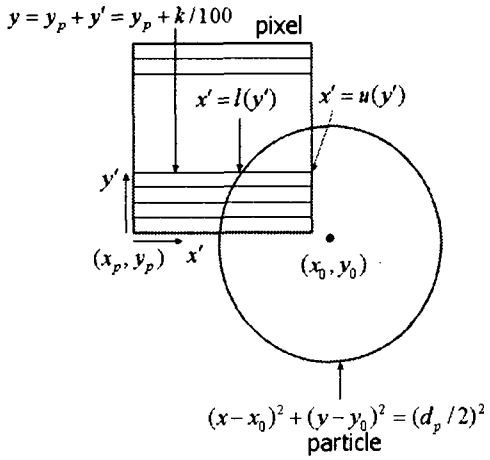

Fig. 3 Intensity quantization

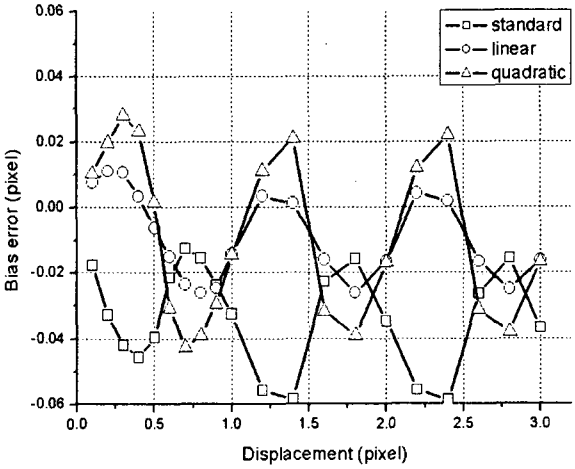

Fig. 4 Standard algorithm, linear and quadratic

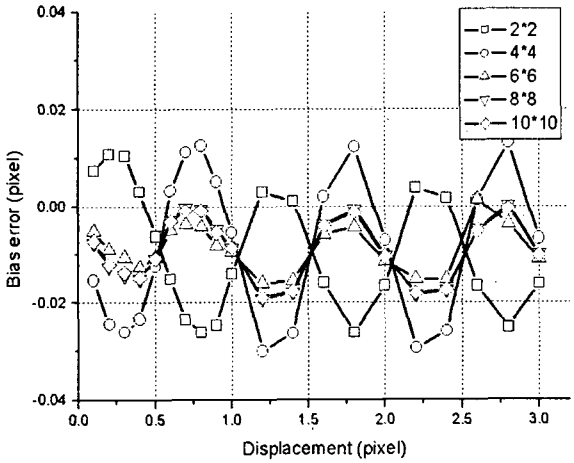

Fig. 5 Truncated sinc interpolation

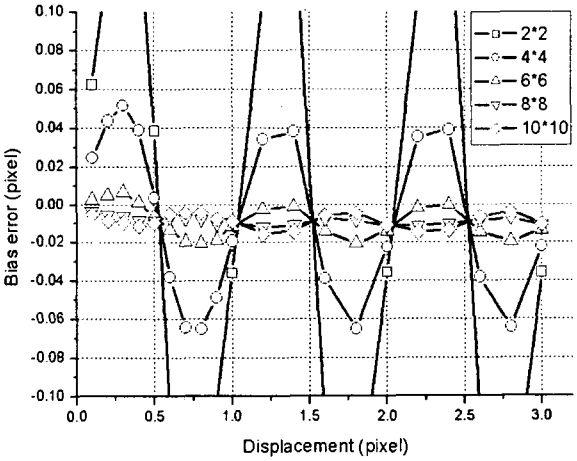

Fig. 6 Windowed sinc interpolations

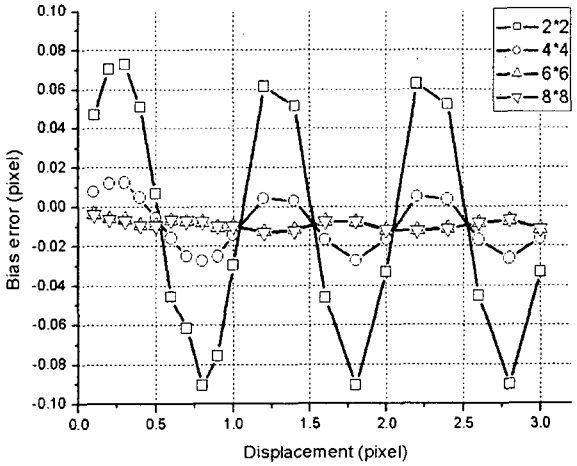

Fig. 7 Cubic interpolations

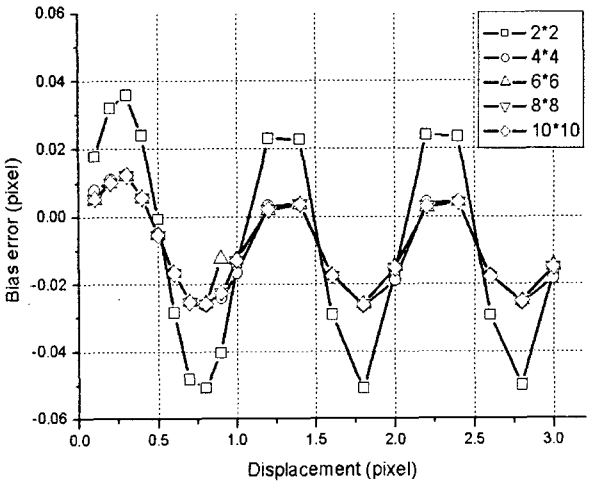

Fig. 8 Gaussian 2nd order interpolation

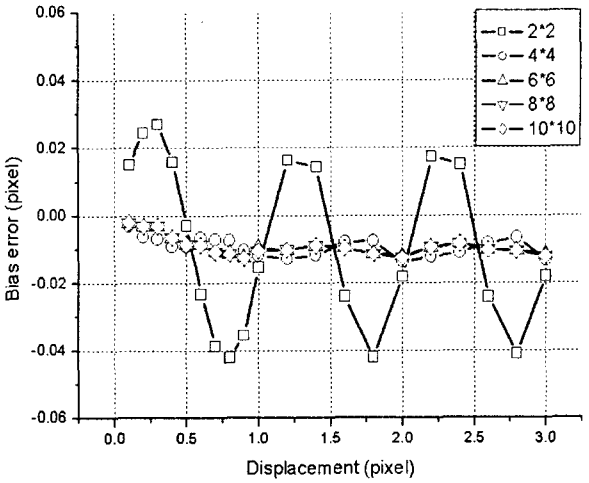

Fig. 9 Gaussian 6th order interpolation

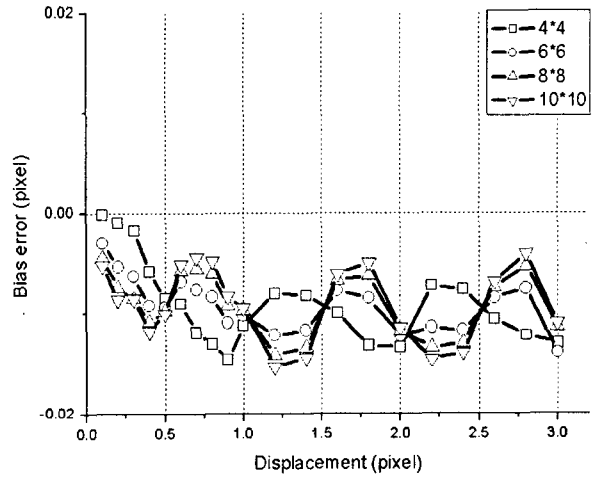

Fig. 10 Lagrange interpolation

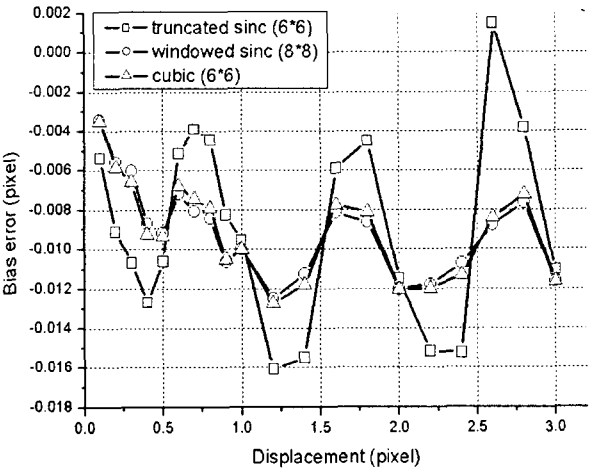

Fig. 11 Comparison of the interpolation with the best kernel size

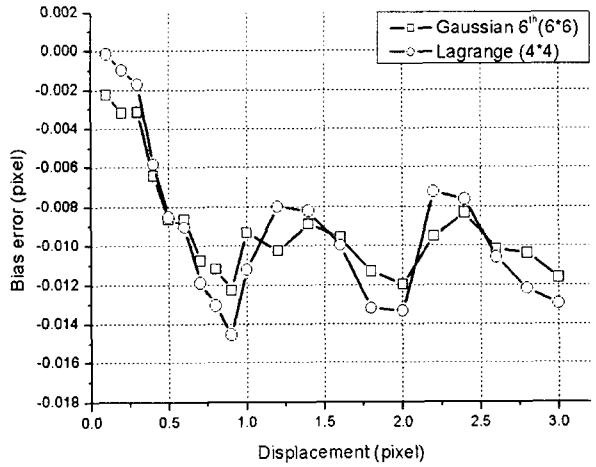

Fig. 12 Bias errors of each interpolation with the best kernel size

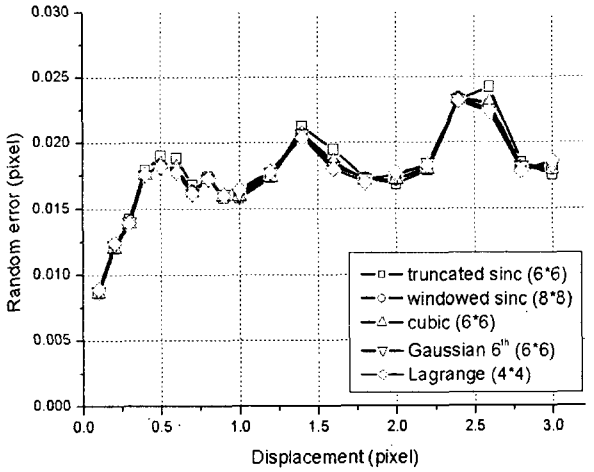

Fig. 13 Random errors of each interpolator with the best kernel size